Nonradiative dynamics of avalanche upconversion in Tm:$LiYF_4$

M. P. Hehlen,* A. Kuditcher, A. L. Lenef, H. Ni, Q. Shu, and S. C. Rand
Division of Applied Physics, 1049 Randall Laboratory, University of Michigan, Ann Arbor, Michigan 48109-1120

J. Rai
Department of Physics, Indian Institute of Technology Kanpur, Kanpur 208016, India

S. Rai
Department of Physics, Indian Institute of Technology Delhi, New Delhi 110016, India

(Received 2 September 1999)

In this paper we examine nonradiative processes (cross relaxation and energy migration) vital for the generation of blue avalanche emission in Tm:$LiYF_4$ crystals subjected to radiation near 648 nm. Time-domain and temperature-dependent measurements indicate that two sequential cross-relaxation processes dominate the nonradiative decays of the $^1G_4$ and $^3H_4$ excited states in this crystal. The occurrence of a sharp peak in the $^3H_4$ fluorescence decay constant versus temperature is reported and explained. Similar behavior is observed in $^1G_4$ emission. Our analysis indicates that individual thermally activated Stark levels dominate cross-relaxation dynamics, revealing unexpected specificity for off-resonant, dark processes in this material. Energy migration in the lower level of the avalanche absorption transition is also sufficiently rapid to explain the magnitude and comparative efficiency of avalanche emission in this material vis-à-vis Tm:YAG. Based on these findings, we predict and experimentally verify the temperature dependence of the threshold pumping intensity for avalanche upconversion in a quantitative manner.

I. INTRODUCTION

Since the discovery of avalanche upconversion,[1] most studies of this intriguing optical phenomenon have concentrated on its radiative aspects. Application of avalanche emission to the generation of short wavelength radiation from long wavelength input enabled the development of novel lasers[2–10] and signal processing capabilities.[11] Recently, avalanche dynamics have permitted the development of high-power upconversion fiber lasers.[12] Very few studies have been performed however on nonradiative aspects of the dynamics, despite the fact that nonradiative steps are rate-limiting steps, which determine the threshold for avalanche upconversion.[13]

The strong, induced absorption on excited-to-excited state transitions that characterizes avalanches has been explained as resonant excited state absorption made possible by a cross-relaxation mechanism facilitated by energy migration. Basic aspects of this picture have been confirmed in recent years.[1,2,7,13,14] Nonradiative steps postulated to sustain and enhance excited-state population, leading to runaway absorption, have not been studied however, since they are difficult to probe. Radiative interactions on absorptive or emissive transitions are easily monitored with standard optical detectors, but the study of nonradiative dynamics like cross relaxation[1] and energy migration[14] is at best indirect, since light is neither absorbed nor emitted during these processes. Consequently few measurements of cross relaxation and migration have been reported in avalanche crystals, and to our knowledge none has previously revealed evidence of a high degree of Stark level specificity in the associated nonradiative dynamics.

Here, results of time-domain degenerate four-wave mixing, luminescence, and transient grating experiments on upconversion in Tm:$LiYF_4$ are presented, which yield a fairly detailed picture of the nonradiative steps of avalanche dynamics in this material (see Fig. 1). First, spectroscopic observations are presented that clarify the assignment for the absorptive avalanche by showing there are two adjacent, yet independent avalanche channels in the 648 nm spectral region. Second, we analyze the observed temperature dependence of $^1G_4$ and $^3H_4$ optical emission to reveal that two main cross-relaxation processes are active in each photon emission cycle of the avalanche process in Tm:$LiYF_4$ in accord with Joubert's surmise for fluoride crystals.[13] Prominent

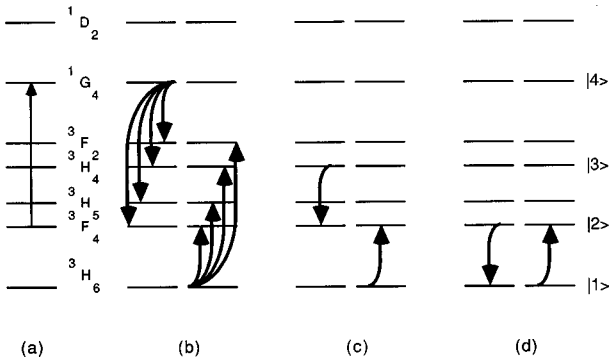

FIG. 1. A schematic diagram of the radiative and nonradiative steps outlined in this paper for avalanche upconversion dynamics initiated on the $^3F_4 \rightarrow {}^1G_4$ excited-state transition of a Tm^{3+} ion. Straight arrows indicate radiative transitions. Curved arrows indicate nonradiative relaxation. (a) Optical excited-state absorption is followed by (b) a first cross-relaxation step (between four potential pairs of multiplets), (c) a second cross relaxation, and (d) energy migration to the reservoir of nearby ground-state ions.

maxima[15,16] occur in rate constants of fluorescent decay at well-defined activation temperatures, revealing observable effects of nonradiative dynamics, which can be reproduced by both a simple model and a numerical computation of cross relaxation having no adjustable parameters. We provide striking evidence that two sequential cross-relaxation processes are involved in sustaining avalanche dynamics in Tm:$LiYF_4$ and that the nonradiative decay from $^3H_4$ is dominated by an interaction between a single Stark level of the excited ion and a single Stark level of the coupled ground state ion.

Direct measurements of energy migration rates in avalanche states are also reported, furnishing a basis for understanding the comparative efficiencies of avalanche emission in Tm:YAG and Tm:$LiYF_4$. In Tm:$LiYF_4$, the dephasing rate observed by photon echo techniques is found to exceed both the cross-relaxation and energy-migration rates, pointing to a direct phonon decay mechanism consistent with the optical transition assignment $^3F_4(3)\rightarrow{}^1G_4(2)$, which begins and ends on excited sublevels. Finally, quantitative agreement is obtained between measurements of the temperature dependence of avalanche threshold and predictions based on the double cross-relaxation model, lending further support to our picture of nonradiative dynamics in Tm:$LiYF_4$.

II. THEORY

Theories on basic aspects of avalanche dynamics have been published previously.[1,2,7] In this section, however, the microscopic origins of temperature dependence and dephasing behavior of avalanche emission in Tm:$LiYF_4$ are considered. Comparisons with experimental results presented later in this paper provide considerable insight into the critical role played by nonradiative processes in meeting the conditions[13] necessary for the occurrence of avalanches in Tm:$LiYF_4$.

Since cross relaxation is vital to avalanche upconversion in all published models, its dependence on temperature should have an important influence on the efficiency and threshold of avalanche dynamics of interest here. Conventional wisdom would suggest that cross relaxation should initiate from the lowest level of excited multiplets (in view of rapid internal relaxation of high-lying sublevels to the lowest—generally metastable—one) and be temperature independent as a pure dipole-dipole coupling process. However, cross relaxation is well known to vary with temperature and we present evidence in Sec. IV that it is a *thermally activated process* in Tm:$LiYF_4$. An activation peak is observed experimentally that is exceptionally high and narrow, indicating that the non-radiative relaxation, which facilitates avalanche emission is very energy- and state-specific. By applying a two-parameter model, one can show that least-square fits to this peak provide adequate energy specificity to discriminate between sets of individual Stark levels that potentially contribute to the cross relaxation of the $^1G_4$ and $^3H_4$ excited states of Tm. This provides a useful tool for assigning specific Stark levels to nonradiative transitions. We then explore possible origins of this specificity through a numerical calculation of vibrationally-assisted dipole-dipole interactions between cross-relaxing atoms and the use of selection rules. In Tm:$LiYF_4$ this quantum mechanical approach yields close agreement with experiment only when the off-resonant, and therefore vibrationally assisted character of the cross relaxation is explicitly taken into account.

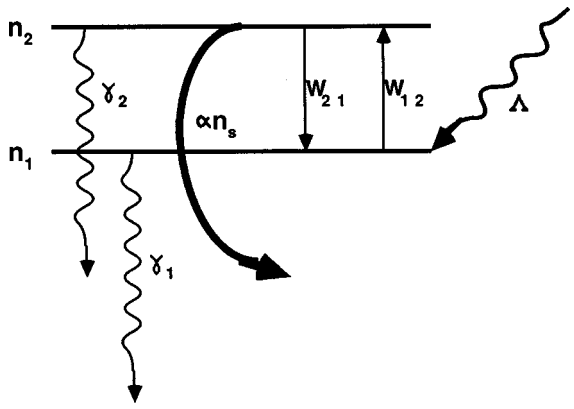

FIG. 2. Empirical model of thermally-activated cross relaxation pertinent to Tm:$LiYF_4$. Only level 1 is populated at rate Λ. It is assumed that radiative decay from Stark sublevels 1 and 2 of the excited multiplet (at rates γ_1 and γ_2) is accompanied by cross relaxation (curved arrow) from state 2 only. Phonon emission and absorption processes are assumed to couple the two levels at rates W_{21} and W_{12}.

A. A simple empirical model

To begin with, we consider a simple model that introduces the concept of thermal activation in a single cross-relaxation process, and consider its potential effect on fluorescence decay. A hypothetical $^{2S+1}L_J$ multiplet consisting of just two Stark sublevels is shown in Fig. 2. Each level decays with a purely radiative rate constant of γ_1 $(i=1,2)$ and phonon-mediated absorption and emission takes place between levels 1 and 2 at the rates W_{12} and W_{21}, respectively. In our model, we make the unusual assumption that cross relaxation can be initiated from level 2 but *not from level* 1. Populations n_1 and n_2 of levels 1 and 2 in the excited multiplet are then described by the rate equations

$$\dot{n}_1 = -\gamma_1 n_1 - W_{12} n_1 + W_{21} n_2 + \Lambda, \tag{1}$$

$$\dot{n}_2 = -(\gamma_2 + \alpha n_s) n_2 - W_{21} n_2 + W_{12} n_1 . \tag{2}$$

In Eq. (1), Λ is an incoherent pumping rate that includes all decay into level 1 by means other than cross relaxation. Equation (2) incorporates cross relaxation through the term $\alpha n_s n_2$, proportional not only to the population n_2 of the excited state in Fig. 2, but also the population n_s of a neighboring ion (not shown) in Stark level s of a different multiplet, assumed to be the ground state. n_s is a constant described by Boltzmann statistics [see Eq. (8)]. The cross-relaxation rate parameter α is generally temperature dependent, as discussed below. The phonon transition rates W_{12} and W_{21} between levels 1 and 2 are also temperature dependent, as discussed by Abragam.[17]

$$W_{12} = \frac{a}{e^{\hbar\omega_{21}/kT} - 1} + bT^7, \tag{3}$$

$$W_{21}=\frac{ae^{\hbar\omega_{21}/kT}}{e^{\hbar\omega_{21}/kT}-1}+bT^7. \tag{4}$$

The first term in Eqs. (3) and (4) describes the ''direct'' phonon contribution. ω_{12} is the splitting between levels 1 and 2 in the excited state. For phonon energies of several hundred cm^{-1}, direct decay is rapid ($W>10^9\,s^{-1}$) at all temperatures of interest in this work, since the coefficient a is quite large (see Sec. V). Radiative decay rates γ_1,γ_2 for levels 1 and 2 and the cross-relaxation parameter α on the other hand are very low, since they depend on transition dipole moments for $4f$-$4f$ intraconfigurational transitions which are very weak. Typical values are $\ll 10^9\,s^{-1}$. The coefficient b determines the magnitude of the ''Raman'' term.

Transient solutions may readily be obtained for this thermal activation model using a compact vector form of the population equations:

$$\dot{\mathbf{n}}=M\mathbf{n}+\Lambda, \tag{5}$$

where

$$M=\begin{pmatrix}-(\gamma_1+W_{12}) & W_{21}\\ W_{12} & -(\gamma_2+W_{21}+\alpha n_s)\end{pmatrix}$$

and

$$\Lambda=\begin{pmatrix}\Lambda\\ 0\end{pmatrix}.$$

The system can be solved with a similarity transformation S that diagonalizes M. The matrix S is

$$S=\begin{pmatrix}\dfrac{W_{21}}{\sqrt{W_{21}^2+(\kappa_1')^2}} & \dfrac{W_{21}}{\sqrt{W_{21}^2+(\kappa_2')^2}}\\ \dfrac{\kappa_1+\gamma_1+W_{12}}{\sqrt{W_{21}^2+(\kappa_1')^2}} & \dfrac{\kappa_2'}{\sqrt{W_{21}^2+(\kappa_2')^2}}\end{pmatrix}$$

and yields a transformed matrix $M'=S^{-1}MS$ of the form

$$M'=\begin{pmatrix}\kappa_1 & 0\\ 0 & \kappa_2\end{pmatrix},$$

where $\kappa_1'=\kappa_1+\gamma_1+W_{12}$, $\kappa_2'=\kappa_2+\gamma_2+W_{12}$, and

$$\kappa_{1,2}=-\tfrac{1}{2}(\gamma_1+\gamma_2+W_{12}+W_{21}+\alpha n_s)\pm\tfrac{1}{2}\sqrt{(W_{12}+W_{21})^2+(\gamma_1-\gamma_2-\alpha n_s)^2+2(\gamma_1-\gamma_2-\alpha n_s)(W_{12}-W_{21})}.$$

The vectors $\mathbf{n}$ and Λ transform according to $\mathbf{n}'=S^{-1}\mathbf{n}$ and $\mathbf{\Lambda}'=S^{-1}\mathbf{\Lambda}$, yielding a transformed equation $\mathbf{n}'=M'\mathbf{n}'+\Lambda'$ with a general solution $\mathbf{n}'=(M')^{-1}[1-\exp(M't)]\Lambda'+\exp(M't)\mathbf{n}'(\mathbf{0})$, equivalent to $\mathbf{n}=SM'^{-1}[1-\exp(M't)]S^{-1}\mathbf{\Lambda}+S\exp(M't)S^{-1}\mathbf{n}(\mathbf{0})$. Explicit expressions for level 1 and 2 populations are

$$\begin{aligned}n_1=&\frac{\Lambda}{(\kappa_2-\kappa_1)}\left[\frac{1-\exp(\kappa_1 t)}{\kappa_1/\kappa_2'}-\frac{1-\exp(\kappa_2 t)}{\kappa_2/\kappa_1'}\right]\\&+\frac{n_1(0)}{\kappa_2-\kappa_1}[\kappa_2'\exp(\kappa_1 t)-\kappa_1'\exp(\kappa_2 t)]\\&+\frac{n_2(0)W_{21}}{\kappa_2-\kappa_1}[\exp(\kappa_2 t)-\exp(\kappa_1 t)]\end{aligned} \tag{6}$$

and

$$\begin{aligned}n_2=&\frac{\kappa_1'\kappa_2'\Lambda}{W_{21}(\kappa_2-\kappa_1)}\left[\frac{1-\exp(\kappa_1 t)}{\kappa_1}-\frac{1-\exp(\kappa_2 t)}{\kappa_2}\right]\\&+\frac{\kappa_1'\kappa_2' n_1(0)}{W_{21}(\kappa_2-\kappa_1)}[\exp(\kappa_1 t)-\exp(\kappa_2 t)]\\&+\frac{n_2(0)}{(\kappa_2-\kappa_1)}[\kappa_2'\exp(\kappa_2 t)-\kappa_1'\exp(\kappa_1 t)].\end{aligned} \tag{7}$$

$n_1(0)$ and $n_2(0)$ specify arbitrary initial populations (for example from pulsed excitation), and Λ otherwise constant, allows for transients that would result from any step change in incoherent pumping at time zero. The dependence on population of ground-state Stark sublevel s is implicit in $\kappa_{1,2}$ through the factor

$$n_s(T)=\frac{n_g}{Z(T)}\exp(-\hbar\omega_s/k_BT). \tag{8}$$

The partition function $Z(T)=\Sigma_{i=1}^{m}\exp(-\hbar\omega_i/k_BT)$ ensures that the total population distributed amongst m sublevels within the multiplet is $n_g=\Sigma_{s=1}^{m}n_s$.

We are interested primarily in the temperature dependence of the population decay rate from level 1. This can easily be measured experimentally from fluorescence decays recorded at different temperatures. By assumption, however, level 1 population decay is limited here by nonradiative decay through state 2. For the 2-level model above in the limit that $W_{12},W_{21}\gg\gamma_1,\gamma_2,\alpha n_s$, the radical in the expression for $\kappa_{1,2}$ can be factored and expanded to first order in $(W_{12}+W_{21})^{-2}$, yielding

$$\kappa_1=\frac{W_{12}\gamma_2+W_{21}\gamma_1}{W_{12}+W_{21}}+\frac{W_{12}\alpha n_s}{W_{12}+W_{21}} \tag{9a}$$

and

$$\kappa_2=W_{12}+W_{21}. \tag{9b}$$

The magnitude of κ_2 greatly exceeds that of κ_1 in systems with slow radiative decay and low αn_s rates. These conditions are commonly met in rare-earth systems over wide ranges of temperature, with the result that populations in

excited states 1 and 2 decay quasiexponentially at the rate κ_1. Hence the core of our model for calculating the temperature-dependent decay rate of excited-state fluorescence consists of Eq. (9a).

For resonant cross relaxation, in which the energy mismatch of two coupled electronic transitions is zero, α should be a constant, independent of temperature. Only very minor changes in α would result from lattice expansion and contraction. However, when nonresonant cross relaxation occurs, phonon emission or absorption must take place to conserve energy overall. For example, a nonradiative decay of excited Tm^{3+} ions via the transition $^3H_4 \rightarrow {}^3F_4$ might occur if accompanied by a $^3H_6 \rightarrow {}^3F_4$ transition of a coupled neighbor, i.e., $[^3H_4, {}^3H_6] \rightarrow [^3F_4, {}^3F_6]$. However this process is highly non-resonant, yielding a minimum excess energy (ΔE) of over 650 cm^{-1} and necessitating the emission of several optical phonons. Consequently, the cross-relaxation coefficient α would acquire a temperature dependence through the probabilities of stimulated absorption or emission of phonons, assumed to be proportional to the product of the corresponding ''direct'' process probabilities.[18]

For dipole-dipole coupling, the purely electronic rate constant for cross relaxation at 0 K [19] is given by

$$\alpha(0)_{ijmn} = \lambda_0 f_{im} f_{jn}. \tag{10}$$

Here f_{im} and f_{jn} are oscillator strengths of $i \rightarrow m$ and $j \rightarrow n$ dipole transitions on the first and second ion respectively. λ_0 is an interaction constant that depends on the separation of the interacting ions and on the integer order of the phonon process $p = \mathrm{Int}(|\Delta E|/\hbar\omega_{\max})$ required to accommodate any large energy mismatch $\Delta E = \hbar(\omega_{im} - \omega_{jn})$ of the electronic transitions mediating the process. $\lambda_0 \propto \exp(-p \ln|\varepsilon|)$, where ε is a strain factor,[20,21] $\omega_{\max}$ is the maximum host phonon frequency available to participate in energy conservation. For a pair of mismatched dipoles, we write the temperature-dependent cross-relaxation coefficient $\alpha(T)$ by multiplying $\alpha(0)$ by the probability of absorption or emission of p phonons of frequency ω_{ph}. This yields

$$\alpha(T) = \alpha(0) \prod_p \frac{(\pm 1)^p}{[\exp(\pm \hbar\omega_{\mathrm{ph}}/k_B T) - 1]}, \tag{11}$$

where the upper $(+)$ sign applies to endothermic and the lower $(-)$ sign to exothermic energy transfer. The order p of the phonon processes is discussed further in Sec. II C.

If cross relaxation from an excited sublevel is more rapid than radiative decay, and multiphonon emission (or absorption) is necessary to conserve energy, then the population decay specified jointly by Eqs. (9) and (11) will exhibit a well-defined peak at the activation temperature. In multilevel systems, the populations of all excited levels increases with temperature, so the effective energy mismatch ΔE can *change* as new transitions become accessible for cross relaxation. If ΔE increases (or decreases), the order p of the multiphonon process necessary to conserve energy must increase (or decrease). This means the probability for an exothermic cross relaxation from an excited state will exhibit a Boltzmann-like increase at low temperatures, but then drop abruptly due to a ''phonon filtering'' effect: higher-order processes are progressively less probable. The position and shape of the intermediate peak are very sensitive to the splittings $\hbar\omega_{21}$ and $\hbar\omega_{s21}$ used in the model, as well as the number of phonons p and their frequency ω_{ph}. In this work we used Eq. (9a) to analyze fluorescence and cross-relaxation decay constants for the $^1G_4$ and $^3H_4$ multiplets of Tm^{3+} ions in highly-doped crystals of Tm:$LiYF_4$, for which accurate crystal field energies are available.[22]

B. Double cross relaxation model

The threshold intensity for avalanche upconversion[23] depends sensitively on nonradiative processes such as cross relaxation. This makes it a useful observable for testing models of nonradiative dynamics. Here we develop a double cross-relaxation model for Tm avalanche dynamics that is later tested by comparison with experimental observations of the threshold over a wide range of temperature.

The avalanche threshold is best defined, and therefore most useful, when ground state absorption (GSA) is negligible, as for Tm^{3+} avalanche transitions observable near 650 nm in many compounds. We introduce a four-level model, which incorporates the double cross relaxation necessary to reproduce our results, and use a simple intersection method to calculate the avalanche threshold versus temperature. This determination is equivalent to the analytic method of Shu[23] and Ni[16] in the limit of negligible GSA, and complementary to that described in Ref. 13.

The population equations for an avalanche system with double cross relaxation are given below. A density matrix description of such dynamics, which includes migration was developed by Ni,[16] but resonant energy migration is not expected to influence the temperature dependence of the avalanche threshold significantly. We show in a later figure (Fig. 12) that Ni's approach provides no noticeable improvement over a rate equation model for threshold prediction, and will not be discussed further. The assumed dynamics correspond to a simple four-level system similar to that shown in Figs. 1(a), (b), and (c), with the four key states identified as $|1\rangle \equiv {}^3H_6$, $|2\rangle \equiv {}^3F_4$, $|3\rangle \equiv H_4$, and $|4\rangle \equiv {}^1G_4$. Migration is ignored for the reason stated above, and populations in excited multiplets other than $|2\rangle$ or $|3\rangle$, such as $^3F_2$ and $^3H_5$ in Fig. 1(b), are assumed to be small as the result of rapid decay to $|2\rangle$ or $|3\rangle$,

$$\dot{n}_1 = \gamma_2 n_2 + \gamma_{31} n_3 + \gamma_{41} n_4 - \mu n_1 n_3 + \mu' n_2^2 - \kappa n_1 n_4 + \kappa' n_2 n_3, \tag{12}$$

$$\dot{n}_2 = BI(n_4 - n_2) - \gamma_2 n_2 + \gamma_{32} n_3 + \gamma_{42} n_4 + 2\mu n_1 n_3 - 2\mu' n_2^2 + \kappa n_1 n_4 - \kappa' n_2 n_3, \tag{13}$$

$$\dot{n}_3 = -\gamma_3 n_3 + \gamma_{43} n_4 - \mu n_1 n_3 + \mu' n_2^2 + \kappa n_1 n_4 - \kappa' n_2 n_3, \tag{14}$$

$$\dot{n}_4 = BI(n_2 - n_4) - \gamma_4 n_4 - \kappa n_1 n_4 + \kappa' n_2 n_3. \tag{15}$$

B is the Einstein absorption coefficient and I is the incident intensity. κ and κ' are coefficients for forward and backward cross relaxation, respectively, of levels 1 and 4, and μ and μ' are the corresponding coefficients for cross relaxation of levels 1 and 3. Steady-state solutions for excited-state populations can be obtained analytically from this set of equa-

tions. Expressions for n_2, n_3, and n_4 are given below,

$$n_2 = d' n_3 + c' n_4, \tag{16}$$

$$n_3 = \frac{[\kappa + \gamma_4 + BI(1-c')] - (1+c')\kappa n_4}{\kappa(1+d')n_4 + BId'} n_4, \tag{17}$$

$$n_4 = \frac{2\sqrt{d^2-3bc}}{3b} \cos\left[\tfrac{1}{3}\cos^{-1}\left(\frac{9bcd - 2d^3 - 27b^2 f}{2(d^2-3bc)^{3/2}}\right)\right] - \frac{d}{3b}. \tag{18}$$

These expressions have been simplified using the following definitions:

$$b = \mu' \kappa^2 (d'-c')^2, \tag{19}$$

$$\begin{aligned} d = {} & [(\gamma_3 + \mu - BId')(1+c')\kappa + (\mu + \mu c' + 2\mu' d' c') \\ & \times (\kappa + \gamma_4 + BI - BIc')]\kappa(1+d') - [\mu(1+c') + 2\mu' d' c'] \\ & \times (1+c')\kappa BId' + [\gamma_{43} - \gamma_4 + BI(c'-1)]\kappa^2(1+d')^2 \\ & + 2\mu'(c')^2 BId'\kappa(1+d') - 2[\kappa + \gamma_4 + BI(1-c')] \\ & \times (1+c')\kappa[\mu(1+d') + \mu'(d')^2], \end{aligned} \tag{20}$$

$$\begin{aligned} c = {} & (-\gamma_3 - \mu + BId')[\kappa + \gamma_4 + BI(1-c')]\kappa(1+d') \\ & + 2BId'\kappa(1+d')[\gamma_{43} - \gamma_4 + BI(c'-1)] \\ & + \mu'(c')^2 B^2 I^2 (d')^2 + [\mu(1+d') + \mu'(d')^2] \\ & \times [\kappa + \gamma_4 + BI(1-c')]^2, \end{aligned} \tag{21}$$

$$\begin{aligned} f = {} & (-\gamma_3 - \mu + BId')[\kappa + \gamma_4 + BI(1-c')]BId' \\ & + [\gamma_{43} - \gamma_4 + BI(c'-1)]B^2 I^2 (d')^2, \end{aligned} \tag{22}$$

$$d' = (\gamma_{31} + \gamma_3)/(2BI - \gamma_2), \tag{23}$$

$$c' = (\gamma_{41} - \gamma_{43} + 2\gamma_4 + 2BI)/(2BI - \gamma_2). \tag{24}$$

The avalanche threshold can easily be predicted from Eq. (16) by numerically or graphically determining the intersection point of $n_2(I)$ with the intensity axis, using linear extrapolation. For accurate predictions however, *experimentally determined* values of the cross-relaxation coefficients must be used at each temperature of interest.[23]

C. Numerical calculations of cross relaxation rates

To explain how thermally activated cross relaxation competes effectively with other decay processes in Tm^{3+}:$LiYF_4$, we turned to a two-part, numerical calculation of cross-relaxation rates with no free parameters. First, oscillator strengths for dipole transitions between individual Stark levels of the $^3H_4$ multiplet were computed, together with those between $^3H_6$ and $^3F_4$ sublevels. This was done with a refined crystal field theory for rare-earth ions[24] due to Reid and others.[25–29] Temperature dependence was then included by considering phonon interactions (up to third order) necessary to conserve energy in each dipole-dipole interaction between atoms, followed by a summation over all levels in the four multiplets. As pointed out in the discussion, this numerical approach yields qualitative agreement with experimental observations and the predictions of the simple model of Sec. II (A), providing support for our conclusions regarding state-specific, thermally-activated cross relaxation in this Tm^{3+} system.

A least squares fit to 52 crystal-field energies[22] (excluding the $^1I_6$ and $^3P_0$ levels) yielded a standard deviation of $\sigma = 17\ \mathrm{cm}^{-1}$ of the eigenvalues with respect to measured energies, using Reid's Hamiltonian in S_4 symmetry. Intensity parameters A_p^λ were calculated[30] from the crystallographic structure of $LiYF_4$ (Ref. 31) and the isotropic fluorine atom polarizability (0.52 Å^3). This provided eigenfunctions that were then used to calculate oscillator strengths for electric-dipole transitions in σ and π polarization between individual Stark levels of different multiplets.

An exhaustive computation of nonradiative decay in $LiYF_4$ should account for crystal structure. However in our calculation, the actual pairwise disposition of rare-earth substituted Y sites in $LiYF_4$ was ignored. To account for it would have required scaling Table I entries for the effective transition moments corresponding to each distinctive pair of dopant ions associated with a given ion at the site origin, based on an assumed model of the distance dependence of their interaction. Products of dipole moments decomposed vectorially into π, σ components with respect to each pair axis in turn could then be averaged for a random distribution of impurities. However, such a computation of site-averaged rates at each temperature is well beyond the scope of this paper.

To obtain the cross-relaxation rate constant numerically at each temperature for only a single pair of ions, oscillator strengths f_{im} and f_{jn} relevant to Eq. (10) were computed between Stark states on each ion. Table I presents oscillator strengths of purely electronic, electric-dipole transitions involved in the $(^3H_6, {}^3H_4) \rightarrow (^3F_4, {}^3F_4)$ cross-relaxation process, calculated as described above. Part (a) of the table refers to $^3H_6 \rightarrow {}^3F_4$ transitions, whereas part (b) refers to $^3H_4 \rightarrow {}^3F_4$ transitions. Values for both σ and π polarizations are included. In this way $\sigma\sigma$, $\sigma\pi$, $\pi\sigma$, and $\pi\pi$ dipole-dipole interaction strengths can be compared with one another and experiment. Cross-polarized interaction rates were not assumed to be zero, despite the apparent orthogonality of their transition axes in the crystal reference frame. The reason for this is that interion axes for most rare-earth pairs in this crystal lie at large angles with respect to the crystallographic axes. Nonzero dipole-dipole interactions can therefore be expected to arise from either σ or π moments with *components perpendicular to the interion axis*. These have large interaction products in the *reference frame of the pair*. Contributions were then summed over all states in the initial and final multiplets, incorporating Boltzmann occupation and phonon factors up to third order to yield the relative probability $P(T)$ of cross relaxation at temperature T:

TABLE I. Calculated oscillator strengths (in units of 10^{-9}) of (a) $^3H_6 \rightarrow {}^3F_4$ and (b) $^3H_4 \rightarrow {}^3F_4$ electric-dipole-allowed crystal field transitions in σ/π polarization for Tm^{3+} in the S_4 site symmetry appropriate for $LiYF_4$. Individual Stark sublevels are specified both by their group representations Γ_1 and (in parentheses) their energies in cm^{-1}. The theoretical fit parameters (in cm^{-1}) used for the energy-level calculation were $F^2=101407$, $F^4=66528$, $F^6=43325$, $\zeta=2614.7$, $\alpha=40.8$, $\beta=-1141$, $\gamma=4476$, $M^0=3.09$, $P^2=-371.9$, $B_{20}=438$, $B_{40}=726$, $B_{44}=-1006$, $B_{60}=-179$, and $B_{64}=795$. The intensity parameters A_{tp}^{λ} (in units of 10^{-11} cm) were $A_{32}^2=-58.3-56.0i$, $A_{32}^4=7.71+7.39i$, $A_{52}^4=-6.80-16.9i$, $A_{52}^6=2.13+5.30i$, $A_{72}^6=-0.14-1.27i$, and $A_{76}^6=5.41+1.17i$.

		$^3F_4$						
		Γ_1 (5599)	Γ_1 (5756)	$\Gamma_{3,4}$ (5757)	Γ_2 (5820)	Γ_2 (5942)	Γ_1 (5968)	$\Gamma_{3,4}$ (5972)
				(a)				
$^3H_6 \rightarrow$	Γ_2 (419)	/4.57	/6.16	2.94/			/0.34	11.2/
	$\Gamma_{3,4}$ (407)	0.60/	1.84/	/5.53	2.60/	22.6/	6.11/	/5.52
	Γ_1 (372)			0.16/	/0.03	/7.74		16.5/
	$\Gamma_{3,4}$ (334)	7.07/	14.2/	/7.51	0.08/	0.04/	8.26/	/29.5
	Γ_1 (319)			2.95/	/4.13	/2.25		13.8/
	Γ_2 (305)	/15.7	/22.4	0.29/			/12.4	0.09/
	Γ_2 (270)	/8.16	/21.5	0.47/			/16.2	2.15/
	Γ_1 (56)			17.2/	/11.4	/0.89		0.19/
	$\Gamma_{3,4}$ (30)	10.8/	0.70/	/15.8	18.5/	0.28/	6.11/	/2.37
	Γ_2 (0)	/2.60	/2.57	18.0/			/2.47	0.35/
				(b)				
$^3H_4 \rightarrow$	Γ_2 (12946)	/5.33	/0.06	16.2/			/10.9	3.46/
	$\Gamma_{3,4}$ (12835)	7.14/	6.92/	/13.3	19.6/	3.25	1.57/	/11.1
	Γ_1 (12835)			0.45/	/2.93	/0.74		7.77/
	Γ_1 (12745)			3.73/	/0.94	/0.09		6.39/
	$\Gamma_{3,4}$ (12643)	0.51/	3.49/	/27.1	0.29/	15.9/	3.53/	/11.7
	Γ_1 (12624)			2.61/	/11.4	/14.8		0.66/
	Γ_2 (12599)	/6.28	/0.42	0.08/			/7.01	20.7/

$$
\begin{aligned}
P(T) &= \sum_{ijmn} n_i n_j \alpha(T)_{ijmn} \\
&= \sum_{ijmn} n_i n_j \alpha(0)_{ijmn} \\
&\quad \times \Bigg[\sum_{q,q'} \exp(-\Delta E_{ijmn}/\hbar\omega_{qq'}) W^{\pm}(\omega_q) W^{\pm}(\omega_{q'}) \\
&\quad + \sum_{r,r',r''} \exp(-\Delta E_{ijmn}/\hbar\omega_{rr'r''}) \\
&\quad \times W^{\pm}(\omega_r) W^{\pm}(\omega_{r'}) W^{\pm}(\omega_{r''}) \Bigg]. \qquad (25)
\end{aligned}
$$

The terms in square brackets give expressions for second-and third-order multiphonon-assisted transitions when $q=q'$ and $r=r'=r''$, respectively.[20,21] For simulation purposes we arbitrarily selected $\ln|\varepsilon|=1$ for the strain factor in λ_0. The q,q',r,r', and r'' indices in the bracketed sums were allowed to run over all $N=26$ observed optical modes (excluding Li motions).[31] However only those terms which achieved a tolerable energy match were retained, as described below. For unequal index values, positive combination frequencies $\omega_{qq'}=\omega_q \pm \omega_{q'}$ and $\omega_{rr'r''}=\omega_{r'} \pm \omega_{r'} \pm \omega_{r''}$ which satisfied the energy conservation condition were also included, in light of recent observations of combination lines in excitation and emission spectra of Yb:$CsCdBr_3$.[32] The +/− signs refer to absorption/emission, respectively. The spectral overlap function, which appears customarily in expressions for dipole-dipole probabilities[33] has been supplanted in Eq. (25) by a product of ''direct'' process factors as in Eq. (11), because of the pronounced (exothermic) energy mismatch in the case at hand.[34] In the $(^3H_6, {}^3H_4) \rightarrow ({}^3F_4, {}^3F_4)$ cross-relaxation process, for example, the $^3H_6 \rightarrow {}^3F_4$ transition terminates in a vibronic sideband region. Its rate is therefore limited by phonon emission rates rather than a purely electronic spectral overlap.

For a fixed value of temperature T, the phonon absorption/emission rates $W^{\pm}(\omega)$ in Eq. (25) can in principle have many values for a given set of electronic state indices i, j, m, and n. More than one set of phonon frequencies can sum to ΔE with a small residual mismatch δ, according to $\Delta E = \hbar(\omega_1 \pm \omega_2 \pm \ldots \pm \omega_p) + \delta$, since any given mode can contribute in principle more than once to a given product. However, in the temperature range 0–50 K, the W rates are nearly constant for all phonon frequencies. When included in the computation of $P(T)$, these factors cause only a slight, monotonic rise at temperatures above 200 K. Hence the approximation $W^{\pm}(\omega)=1$ was introduced to save computation time. Only frequency combinations which reduced δ to a value less than the Debye energy[35] were retained, since this energy defect can be accommodated within the continuum of acoustic phonons. Even so, some 10^9 terms had to be evalu-

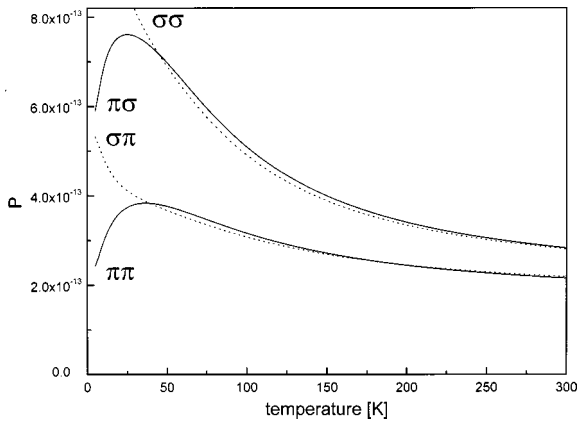

FIG. 3. Probability of the cross-relaxation process $(^3H_4, {}^3H_6) \rightarrow (^3F_4, {}^3F_4)$ vs temperature, calculated numerically from theoretical oscillator strengths for state-specific transitions, using Eq. (25), taking all sublevels of the multiplets $^3H_4$, $^3H_6$, and $^3F_4$ into account. Separate curves are displayed for $\sigma\sigma$ (solid line) and $\pi\pi$ (dashed line) polarizations of the dipole-dipole interaction.

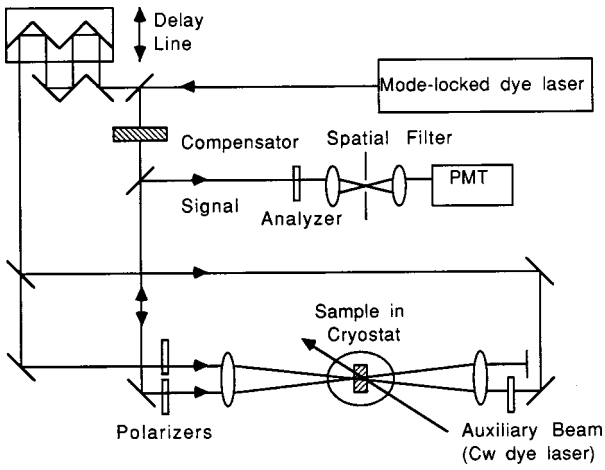

FIG. 4. Experimental layout for dephasing measurements using the 3-pulse stimulated photon echo technique in a counter-propagating pump pulse geometry. A weak auxiliary cw laser beam was used to maintain a steady population in the avalanche level probed by the ultrafast pulses.

ated for each of 150 temperatures to plot curves for each polarization.

The temperature dependence computed in this way from Eq. (25) is shown in Fig. 3, with separate curves for $\sigma\sigma$-, $\sigma\pi$-, $\pi\sigma$-, and $\pi\pi$-polarized interactions. The first label for each of these dipole-dipole interactions specifies the polarization of the ion making the downward transition from an excited electronic multiplet. As discussed later, these results serve to justify the unprecedented assumption of the simple model represented by Eq. (9a). This establishes the physical basis on which to extend this kind of analysis to anomalous decays observed from other states (like $^1G_4$), and thermally-activated cross relaxation in other systems.

III. EXPERIMENTS

Polarized excitation spectra of blue avalanche emission from $^1G_4$ were first recorded with a 1-meter spectrograph, using light from a cw dye laser operating in the spectral range 620–650 nm. The spectra revealed wavelengths which were effective in generating strong avalanche emission at various temperatures between 30–295 K, namely, 648.9 nm $[^3H_4(3) - {}^1D_2(3)]$, 648.2 nm $[^3F_4(3) - {}^1G_4(2)]$ and 628.3 nm $[^3F_4(1) - {}^1G_4(5)]$. All transitions were π-polarized in agreement with group theoretical selection rules for the sublevel assignments in parentheses.[36] The transition at 648.2 nm had the lowest threshold. Hence it was selected for the additional measurements reported here.

Next, time-resolved photoluminescence decay measurements were made for the $^1G_4$ and $^3H_4$ states of Tm. In the case of $^1G_4$, optical excitation was provided by a combination of Ti: sapphire and DCM dye laser sources on the $^3H_6 \rightarrow {}^3H_4$ and $^3F_4 \rightarrow {}^1G_4$ transitions at 781 nm and 648 nm, respectively. Detection was provided by a 1P28B photomultiplier preceded by a 480 nm interference filter. Emission from $^3H_4$ was excited by the dye laser alone, on the $^3H_6 \rightarrow {}^3F_2$ transition at 659 nm, and was detected through a Corning 7-59 glass filter. In both cases, fast solid state switches were used to gate a frequency synthesizer whose amplified output drove an acousto-optic modulator, thereby controlling the intensity of dye laser light reaching the sample. The driver output consisted of a square wave of 200 ms period. Impulse response times of 60 ns were easily achieved, and were more than adequate for recording micro- and milli-second decay times of Tm on the trailing edge of each pulse.

Flourescence decay signals for the $^1G_4$ and $^3H_4$ states were recorded over a wide temperature range between 5–300 K using this approach. Cross-relaxation rates were determined as a function of Tm ion concentration at room temperature by measuring $^3H_4$ decay times in four samples containing 1.5, 3.1, 4.8, and 8.2 mol. % Tm under identical conditions, and simply subtracting the Judd-Ofelt radiative rate of 515 s^{-1}.[22] Absolute concentrations were estimated to be accurate to only about 25%, whereas the relative concentrations of these samples were established spectroscopically to within $\pm 0.1\%$ by comparing absorption line strengths at 659 nm under identical conditions. The high accuracy of relative doping levels was vital for reliably determining the concentration dependence of the cross-relaxation rate.

Optical dephasing measurements were made using degenerate four-wave mixing (DFWM) techniques on the $^3F_4(3)$-$^1G_4(2)$ excited-state transition. This provided additional information on the avalanche mechanism. As shown in Fig. 4, the output of a cavity-dumped, cw mode-locked DCM dye laser was divided into three beams in a counter-propagating pump geometry. The second harmonic autocorrelation width was 1.02 ps, corresponding to a Gaussian pulse width of approximately 700 fs. A computer-controlled, optical delay line was used to control the relative timing of the pulses incident on the sample. Use of a position-sensitive detector during alignment of the delay stage rendered beam displacement errors negligible for delays of up to ± 7 ns.[37] The phase conjugate signal intensity was recorded as the delay between the first two pulses was varied in such a way that the delay between pulses two and three remained constant. For all dephasing measurements, the ultrafast dye laser intensity was maintained well below avalanche threshold ($<$80 mW or 1.0 kW/cm^2), with a three-beam total input of less than 10 mW. Avalanche conditions were adjusted by

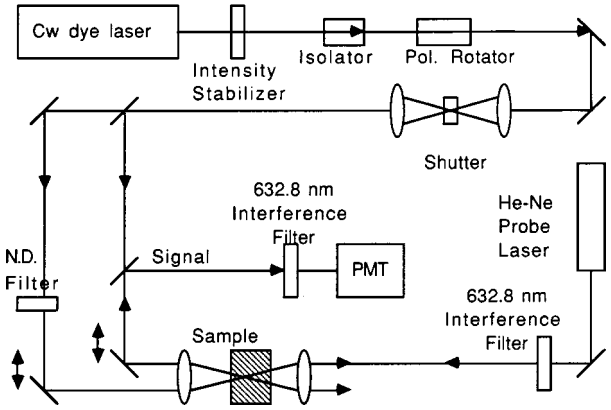

FIG. 5. Experimental setup for transient grating observations to measure energy migration rate in the $^3F_4$ state of Tm^{3+} ions in $LiYF_4$ and YAG. Intense dual-beam excitation on the excited-state absorption transition $^3F_4 \rightarrow {}^1G_4$ generates an index grating due to avalanche population of the $^3F_4$ state, which is then probed by diffraction of a He-Ne beam.

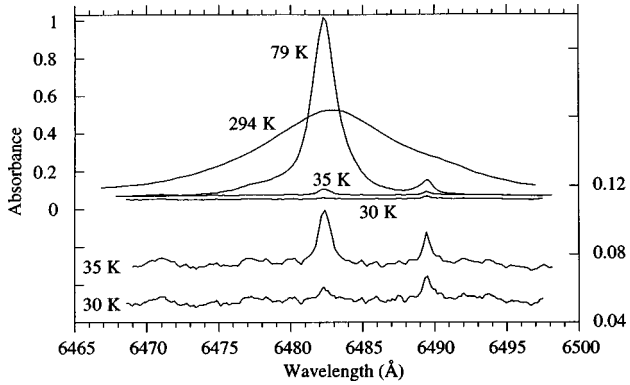

FIG. 6. Induced (avalanche) absorption spectra of Tm upconversion emission (detected in the range $\lambda_{em}=300-500$ nm) at various temperatures between 30–300 K. The two features at 648.2 and 648.9 nm overlap at high temperature, but are distinct and intensity reversed below 35 K (lower trace).

varying the intensity of an auxiliary single-mode dye laser tuned to 648.23 nm. With this arrangement, the dephasing rate could be probed as a function of auxiliary laser power. The pulsed laser bandwidth was broad enough to overlap two neighboring avalanche transitions at 648.2 and 648.9 nm, as described in the next section. However the negligible bandwidth ($\sim$1 MHz) of the auxiliary laser and deliberate tuning of both laser sources to the short wavelength feature at 648.2 nm restricted DFWM measurements to the desired avalanche.

The rate of spatial migration of energy among Tm ions in the $^3F_4$ level of a 5% Tm:$LiYF_4$ crystal was also measured by a transient grating technique.[38] As indicated in Fig. 5, the intensity of a He-Ne beam scattered by the excitation grating of two crossed pump beams at 648.2 nm was measured, after the pump beams were switched off. In this particular sample, populating the $^3F_4$ level by avalanche absorption was equivalent to direct excitation because the lifetimes of populations in higher states were considerably shorter than either the $^3F_4$ radiative lifetime or the measured grating decay time. The probe light was focused more tightly than the pump beams (through the use of 25 cm and 35 cm focusing lenses, respectively) to ensure uniform sampling of the interaction region. The crossing angle θ was varied experimentally by translating mirrors, which varied the separation of two parallel writing beams impinging on a common focusing lens. By plotting the decay rate of diffracted intensity versus θ in the usual way,[38] the energy diffusion coefficient D was determined.

Finally, the threshold intensity for avalanche emission was investigated as a function of temperature between 50–300 K. Measurements were made by recording transmission as a function of power in the range 0–400 mW at each temperature. Then, the graphical intersection between the asymptote of the power-dependent transmission and the low-power transmission limit was determined. In all, threshold values for eleven different temperatures were obtained in this way.

IV. RESULTS

Excitation spectra recorded at various temperatures in the range 30–300 K revealed that two strong, independent avalanches existed in the neighborhood of 648 nm in Tm:$LiYF_4$. Figure 6 shows that π-polarized, induced-absorption features occur at 648.9 nm $[^3H_4(3) \rightarrow {}^1D_2(3)]$ and 648.2 nm $[^3F_4(3) \rightarrow {}^1G_4(2)]$. Below 100 K, the independence of these two induced features was manifested by their spectral separation and the reversal of their relative intensities at liquid helium temperatures. At room temperature where these features overlapped, care was necessary to avoid exciting both processes. All our experiments were performed by tuning precisely to the 648.2 nm line with the use of a wave meter.

Results for the temperature dependence of $^1G_4$ flourescence decay rate are given in Fig. 7. This data exhibited an increase with temperature that peaked at 200 K. The same was true for fluorescence from the $^3H_4$ state, though the peak was at 30 K and more pronounced (Fig. 8). However in both cases the solid curves, which are fits based on Eqs. (9a) and (11), reproduced the observations very well. The empirical fit for $^1G_4$ assumed that decay originated from the lowest crystal field level of the excited multiplet and made use of

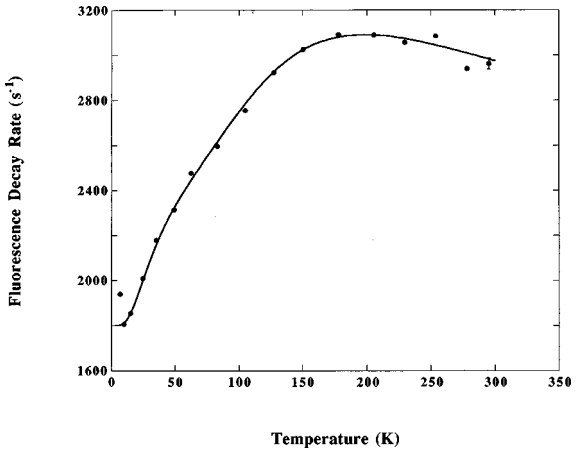

FIG. 7. Fluorescence decay rate vs temperature for $^1G_4$ emission in 1.5% Tm:$LiYF_4$. The $^1G_4$ radiative decay rate from Judd-Ofelt theory is 849 s^{-1}. The solid curve is the best fit of Eq. (9a), applied to the sum of the three cross-relaxation processes $[^1G_4(1), {}^3H_6(2,3,4)] \rightarrow [^3H_4(3), {}^3H_5(1,2,3)]$, ignoring phonon emission/absorption.

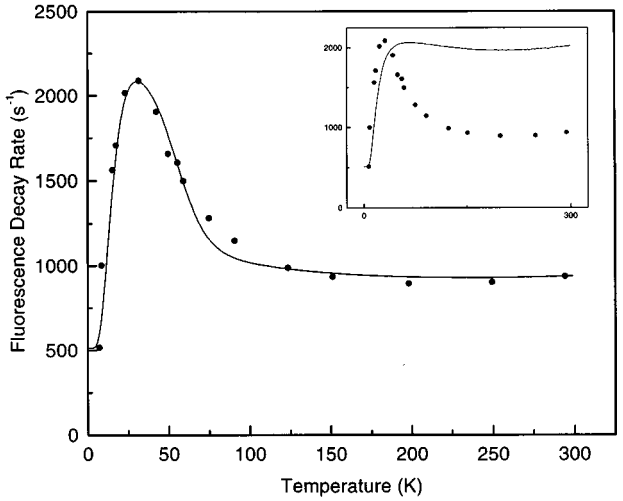

FIG. 8. Fluorescence decay rate vs temperature for $^3H_4$ emission in 1.5% Tm:$LiYF_4$. The $^3H_4$ radiative decay rate from Judd-Ofelt theory is 515 s^{-1}. The solid curve is the best fit of Eq. (9a), applied to the cross-relaxation process $[^3H_4(2), {}^3H_6(1)] \rightarrow [^3F_4(5), {}^3F_4(6)]$ accompanied by the emission of two 329 cm^{-1} phonons. Inset: Example of the much poorer fit obtained by assuming cross relaxation initiated from the second ground-state sublevel (i.e., for the process $[^3H_4(2), {}^3H_6(2)] \rightarrow [^3F_4(5), {}^3F_4(6)]$).

three ground-state levels on the neighboring coupled atom, namely, the 30, 56, and 270 cm^{-1} sublevels of $^3H_6$. The fit for $^3H_4$ cross relaxation made use of only a single excited crystal field level at 12624 cm^{-1} and the ground-state level at 0 cm^{-1}.

The $^3H_4$ cross-relaxation rate was also measured as a function of Tm concentration in four crystals. This dependence was determined by fitting (Fig. 9) the fluorescence decay times to the formula $\tau^{-1} = \tau_0^{-1} + c(\rho_{\mathrm{Tm}})^m$, where τ_0 is the radiative decay time, ρ_{Tm} is the Tm dopant density and c is a constant. This yielded $m = 2.36 \pm 16$. As indicated by the error bars, the largest uncertainties were associated with the rate determination rather than the concentrations. Relative

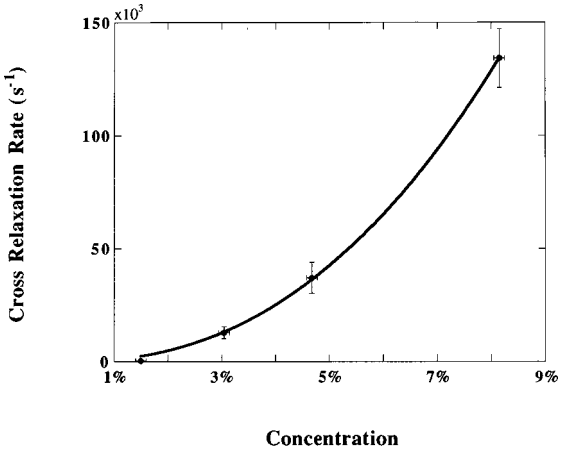

FIG. 9. Nonradiative decay rate (fluorescence rate minus the radiative rate 515 s^{-1}) of the $^3H_4$ state in 1.5% Tm:$LiYF_4$ at room temperature. The solid curve is the best fit to the formula $\tau^{-1} = c(\rho_{\mathrm{Tm}})^m$ with $m = 2.36 \pm 0.16$.

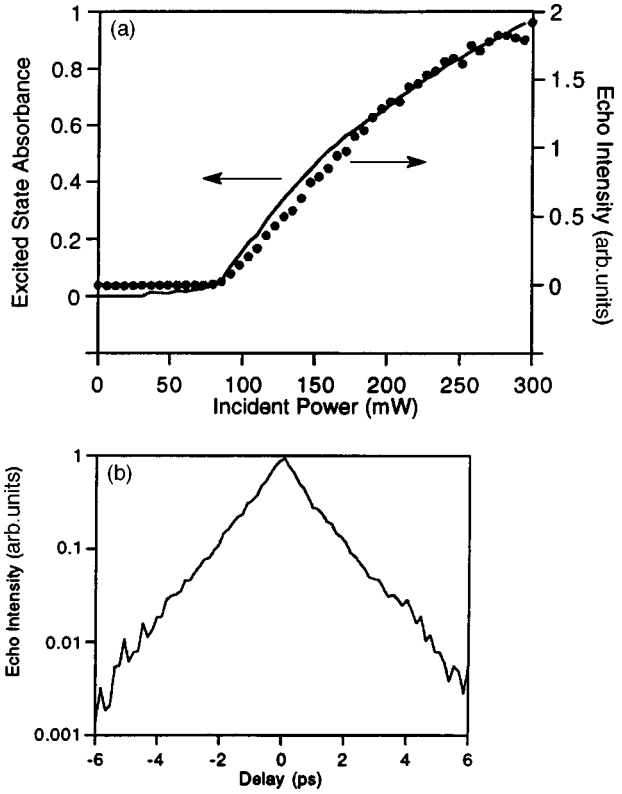

FIG. 10. (a) Degenerate four-wave mixing (DFWM) signal intensity vs auxiliary cw pump power at $\lambda_{\mathrm{CW}} = 648.23$ nm, resonant with the $^3F_4(3) \rightarrow {}^1G_4(2)$ avalanche transition in 10% Tm:$LiYF_4$ ($T = 77$ K). The solid curve is the measured excited-state absorbance ($T = 77$ K). (b) DFWM signal vs delay between first and second pulses ($T = 60$ K). Time interval between pulses 2 and 3 was 1.5 ns. Auxiliary pump intensity was 100 kW/cm^2. A least-squares fit to semilogarithmic decay yielded $T_2 = 1.81 \pm 0.02$ ps. The presence of symmetry with respect to zero delay indicates homogeneous broadening and, strictly speaking, a free polarization decay rather than an echo.

concentrations were determined with respect to the most dilute sample (1.5%) from precise spectroscopic ratios of measured ground-state absorption coefficients in these samples.

Figure 10 presents four-wave mixing (FWM) results for a 10% Tm:$LiYF_4$ crystal at 77 K. In Fig. 10(a), the signal intensity is shown to exhibit the same threshold as avalanche emission, indicating that the measurements were indeed sensitive only to the excited state avalanche dynamics. The FWM signal strength is in fact proportional to the induced excited state absorbance. Fig. 10(b) shows that the dephasing time at 60 K in the same crystal was $T_2 = 1.81 \pm .02$ ps due to a homogeneous mechanism, in view of the right-left symmetry of the data with respect to zero delay. The dephasing time was much shorter than either the radiative lifetime of the $^1G_4$ state or its cross-relaxation decay time. Unfortunately, dephasing times were faster than the system resolution at higher temperatures and higher incident intensities, so the dephasing behavior versus temperature and intensity could not be deduced reliably, unlike Tm:$YAlO_3$.[39]

Figure 11 presents data on the decay rates of avalanche gratings versus writing angle θ. Shu showed that these gratings are primarily dispersive in Tm:$LiYF_4$, despite their resonant character.[23] In Fig. 11(a), the data for the $^3H_4$ state

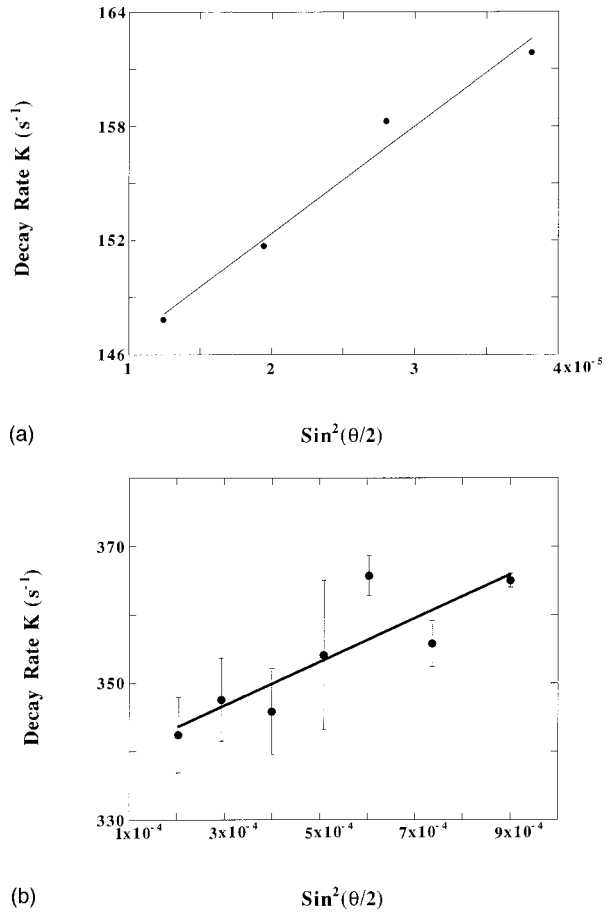

FIG. 11. Dependence of the transient grating decay rate K on spatial period of the excitation grating. Solid lines are best fits to $K=2/\tau+32(\pi/\lambda)^2 D\sin^2(\theta/2)$, where τ is the fluorescence decay time and $\theta/2$ is the crossing half-angle, which determines grating wavelength. (a) Results for 5% Tm^{3+}:$LiYF_4$, and (b) results for 4% Tm^{3+}:YAG at room temperature. Possible errors in (a) are comparable to those shown in (b).

have been plotted so as to permit an easy determination of the diffusion coefficient D from the slope of the graph. This yielded a value of $D=(7.5\pm0.8)\times10^{-6}$ cm^2/s. A similar determination [Fig. 11(b)] for 4% Tm:YAG gave the considerably lower value of $D=(4.7\pm1.2)\times10^{-7}$ cm^2/s.

Finally, the results for avalanche threshold versus temperature in a 1.5% Tm:$LiYF_4$ crystal are presented in Fig. 12. This data shows the minimum values of optical power in a fixed focus geometry, which were necessary to initiate avalanche emission at the designated temperatures. An obvious minimum appeared in this plot near 110 K. This temperature fell between the two temperature maxima observed in the nonradiative decay rates of the $^1G_4$ and $^3H_4$ manifolds (Figs. 7 and 8). The significance of this observation is discussed further in the next section.

V. DISCUSSION

The observed peaks in the decay data of Figs. 7 and 8, taken together with the evidence for quadratic Tm^{3+} ion density dependence of the $^3H_4$ relaxation given in Fig. 9, make it apparent that the $^1G_4$ and $^3H_4$ states in Tm^{3+}:$LiYF_4$ relax

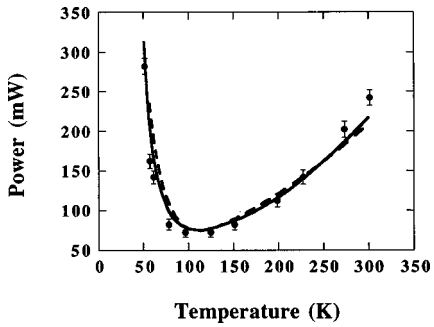

FIG. 12. Avalanche threshold vs temperature in 1.5% Tm^{3+}:$LiYF_4$ for cw excitation at $\lambda=648.2$ nm. Experimental points are shown with dots and the solid curve is a best fit obtained by rate equation analysis of the double cross-relaxation model described in the text. The dashed curve includes energy migration[16] but does not significantly improve the fit.

by thermally activated, *nonradiative* processes. This is very surprising.

Radiative decay constants are temperature-independent, as the name implies. Hence thermal population of excited sublevels normally yields monotonic variations in total population decay rate versus temperature for an excited multiplet,[40] and variations are linear in the density. The results reported here cannot be understood on this basis. It is therefore significant that a simple analytic (empirical) model of cross relaxation, postulating thermal activation through specific excited Stark levels (solid curves in Figs. 7 and 8) provides an excellent description of peaks in the measured flourescence decay rates versus temperature, as well as their quadratic density dependence. We first discuss the implications of our model for determining candidate transitions of cross-relaxation processes in Tm:$LiYF_4$, finding that analysis of $^1G_4$ decay is less definitive than that for $^3H_4$. We then consider how it is possible for state-specific interactions to play important roles in nonradiative dynamics.

The $^1G_4$ decay rate (Fig. 7) exhibited a very broad peak as temperature increased. The breadth of the peak alone argues against any energetic specificity in the nonradiative process governing the temperature dependence. Consequently, it should not be surprising that this data resists analysis until it includes several candidate processes with energy levels, which simultaneously conserve energy within $\Delta E<50\,\mathrm{cm}^{-1}$ and span the appropriate thermal activation range: $[^1G_4(1),\ ^3H_6(2,3,4)]\rightarrow[^3F_2(1,2,3),\ ^3F_4(2,3,4,5)]$, and $[^1G_4(1),\ ^3H_6(2,3,4)]\rightarrow[^3F_4(3,4),\ ^3F_2(2,3,4)]$ and $[^1G_4(1),\ ^3H_6(2,3,4)]\rightarrow[^3H_4(3),\ ^3H_5(1,2,3)]$. These processes, sketched in Fig. 13(b), have the smallest energy defects on $\pi\pi$ or $\sigma\sigma$ allowed-dipole transitions. There are many others (>40) with somewhat larger defects. The width of the $^1G_4$ peak was too great to constrain the model adequately on the basis of thermal activation behavior to assign excited state multiplets more precisely. Nevertheless, fits were significantly affected by restrictions on which ground-state Stark levels were included in the expression for n_s. The best fit was obtained when the subset $^3H_6(2)$, $^3H_6(3)$, and $^3H_6(4)$ was incorporated in the expression for n_s, yielding the curve shown in Fig. 7, and it was necessary to exclude the lowest Stark level $^3H_6(1)$ to obtain good agreement. However, without further information with which to analyze

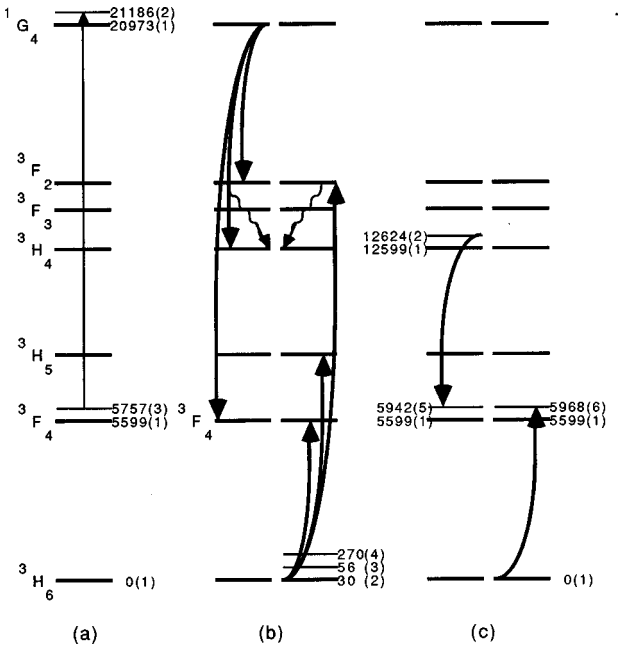

FIG. 13. Details of the avalanche process in Tm^{3+}:$LiYF_4$. Stark level assignments are shown for (a) the optical transition, as well as (b) the first, and (c) second cross-relaxation steps.

this process or independent evidence of more specificity in the dynamics, our picture of relaxation in the Tm system must retain the multiplicity of transitions indicated in Fig. 13(b) as possible components of the first cross relaxation responsible for avalanche upconversion in Tm:$LiYF_4$.

In the case of $^3H_4$ decay, no combination of electronic transitions conserves energy to better than 650 cm^{-1}. It therefore seemed reasonable to identify the final multiplet as the one minimizing the order of the vibrational process required to conserve energy. This greatly reduced the number of candidate transitions for cross relaxation. Additionally, measurements of $^3H_4$ decay rate versus temperature (Fig. 8) showed a much narrower and more prominent peak than $^1G_4$ decay. To fit the wide-ranging $^3H_4$ data from a more limited set of candidate transitions, it was found necessary to restrict the state selection for the 2-parameter model to a single set of Stark levels, namely, $[^3H_4(2), {}^3H_6(1)] \rightarrow [^3F_4(5), {}^3F_4(6,7)]$. The corresponding dynamics are illustrated in Fig. 13(c), and we elaborate on this assignment below. Only by requiring that the upward transition from $^3H_6$ terminates in a vibrational sideband of $^3F_4$ were we able to model depopulation of $^3H_4$ by a pair process, satisfy a $\pi\pi$-type dipole-dipole selection rule and simultaneously reproduce the observed temperature dependence of fluorescence decay.

There can be little doubt that $^3H_4$ decay is pair-mediated, in view of the direct evidence presented in Fig. 9, in the form of quadratic dependence of fluorescence decay on Tm ion concentration. Hence the simple model of Sec. II A is an appropriate starting place for the analysis of nonradiative decay measurements over a wide temperature range. The solid curve in Fig. 8 used the ratio a/b and the cross-relaxation coefficient λ_0 as the only adjustable parameters to do this. Acceptable fits were obtained over very limited ranges of these input parameters, and failed altogether to reproduce the data when initial states other than $^3H_6(1)$ and $^3H_4(2)$ were used in the model (see Fig. 8 inset). The rapid rise in the rate constant plotted in Fig. 8 between 0–30 K was well reproduced by thermal activation of the $^3H_4(2)$ level. The rapid fall on the high-temperature side of the peak was governed by the exponential dependence on energy mismatch in Eq. (11), as higher-lying levels of the excited multiplet became populated. The ratio of Raman to direct contributions affected primarily the slow, monotonic rise observed near room temperature.

In making the final assignment in Fig. 13(c), the polarizations of the transitions comprising $^3H_4$ cross relaxation were assumed to be either $\pi\sigma$ or $\pi\pi$. According to the numerical results in Fig. 3, only $\pi\sigma$ and $\pi\pi$ polarizations result in temperature curves with appropriate peak positions and acceptable contrast. The $\sigma\sigma$ and $\sigma\pi$ calculations showed no peak at all. On this basis we argue that although the $\sigma\sigma$ process $[^3H_4(2), {}^3H_6(1)] \rightarrow [^3F_4(7), {}^3F_4(7)]$ has an energy defect (680 cm^{-1}) that is smaller than that of $[^3H_4(2), {}^3H_6(1)] \rightarrow [^3F_4(5), {}^3F_4(6,7)]$ comprised of $\pi\pi(\Delta E = 714\,cm^{-1})$ and $\pi\sigma(\Delta E = 710\,cm^{-1})$ transitions, it does not appear to account for the activation data. The next nearest allowed transition terminating in the $^3F_4$ multiplet increases ΔE by more than 200 cm^{-1}. For this reason, Fig. 13(c) identifies the $^3H_4$ cross relaxation process as $[^3H_4(2), {}^3H_6(1)] \rightarrow [^3F_4(5), {}^3F_4(6,7)]$.

DFWM measurements permitted rough estimation of the rapid phonon thermalization rate constant a used in numerical and model calculations. The dephasing time T_2 measured at 648.2 nm [Fig. 10(b)] corresponded to a dephasing rate of $\Gamma = 1.76 \times 10^{11}\,s^1$ at $T = 60$ K, consistent with the assignment $[^3F_4(3) - {}^1G_4(2)]$ of the avalanche transition, which begins and ends on excited Stark levels and should indeed decay rapidly by phonon emission. By assuming $W \cong \Gamma$, the value $a = 2.9 \times 10^{13}\,s^{-1}$ was estimated from Eq. (3). The value of a/b determined from a best fit (Fig. 8) of the simple model of Sec. II A to the activation data was 4.6×10^9. The a/b ratio and λ_0 were the only quantities treated as free parameters to obtain the solid curve in Fig. 8.

While the thermally activated cross-relaxation model can evidently reproduce the unusual decay curves for the $^1G_4$ and $^3H_6$ states, there is no precedent of which we are aware explaining how state-specificity arises in a cross-relaxation process. In this regard, the results of the numerical calculation of cross-relaxation rate based on Eq. (25) from Sec. II B are helpful. *With no free parameters*, the theoretical results for both $\pi\sigma$ and $\pi\pi$ polarizations (Fig. 3) showed low-temperature peaks whose position and shape were in very reasonable agreement with $^3H_4$ cross-relaxation data. Yet the entries in Table I do not reveal any obvious reason why thermally activated transitions should dominate the cross-relaxation behavior. In this regard, it was useful to consider two limiting cases of the numerical computation described in Sec. II C. For $\alpha = \text{const}$, a broad, barely discernible peak around 50 K and a plateau at higher temperatures was predicted for $\sigma\sigma$-polarized interactions. A similar plot for $\pi\pi$-interactions yielded no peak at all, showing a monotonic increase over the same temperature range, with only slight inflections at temperatures corresponding to the lowest Stark level energies in the $^3H_4$ and $^3H_6$ multiplets. This calculation reproduced the rapid rise in cross relaxation between 0–30 K, showing that thermal activation in Tm:$LiYF_4$ is electronic in origin. However, it failed altogether to predict

the precipitous decrease at higher temperatures. For $\alpha = \alpha(T)$ as in Eq. (25), the introduction of energy-conserving vibrational interactions generated the observed downturn. Participation of low-lying sublevels of the $^3H_4$ and $^3H_6$ multiplets with large dipole moments was particularly favored on transitions to $^3F_4$. Vibrational sideband absorptions requiring three or more phonons were strongly disfavored, indicating that phonons ''filter out'' many potential pathways for cross relaxation. We propose the occurrence of large dipole moments in the lowest excited sublevels, combined with vibrational exclusion of higher-lying sublevels as the main source of state specificity in $^3H_4$ decay of Tm:$LiYF_4$.

Energy migration in the $^3F_4$ avalanche state of Tm^{3+} was found to be very rapid in both 5% Tm:$LiYF_4$ and 4% Tm:YAG [Figs. 11(a) and 11(b)]. Taking the average separation of Tm ions to be the inverse cube root of Tm density ($d = 1.13$ nm in 5% Tm:$LiYF_4$), the diffusion constant D determined by the transient grating technique was converted to an estimated migration rate according to $\beta = D/d^2$.[38] This procedure gave $\beta = (5.9 \pm 0.3) \times 10^8\ s^{-1}$ for $LiYF_4$. A similar estimate for 4% Tm:YAG, in which the average dopant ion separation is $d = 1.22$ nm, yielded a migration rate of $\beta = (3.2 \pm 0.9) \times 10^7\ s^{-1}$. Hence migration was found to be much faster in $LiYF_4$ than YAG. The product of migration rate times energy level lifetime is the migration enhancement factor of Ni.[14,16] This factor expresses the ratio of the number of photon absorption cycles possible with and without migration in the avalanche level of a selected dopant ion. Using theoretical values[22] for τ of 12 and 11 ms, respectively, the enhancement factors for Tm:$LiYF_4$ and Tm:YAG were calculated to be 7×10^6 and 4×10^5. This factor accounts for the order of magnitude greater efficiency of avalanche emission in $LiYF_4$ host crystals compared to YAG.

Finally, using the picture of double cross relaxation developed in this paper, and the intersection method described in Sec. II A, the temperature dependence of the avalanche threshold was predicted. Judd-Ofelt calculations provided the necessary radiative decay rates. Values for μ and κ were obtained by subtracting radiative rates from the measured totals in Figs. 7 and 8, and we assumed $\mu' = \mu$ and $\kappa' = 0$. The B coefficient for the avalanche transition was estimated from the excited-state linewidth[36] to be $8.6 \times 10^{-6}\ s^{-1}\ m^2/W$. To account for thermal occupation of the initial avalanche state $^3F_4(3)$, we also replaced n_2 by $n_2 \exp(-\hbar\omega_{31}/k_BT)/Z$ in Eqs. (12)–(15), where $\hbar\omega_{31} = E_3 - E_1$ is the splitting of Stark level 3 with respect to the lowest level. Excellent agreement with experiment was obtained, as shown in Fig. 12. The occurrence of a minimum in the threshold data at 110 K clearly reflected a balance between maximization of the rates for two main processes, a cross relaxation whose rate peaked at a temperature of 195 K and a second step which peaked at 30 K. Agreement between theory and experiment therefore provided additional support for the analysis of nonradiative dynamics underlying the avalanche process in Tm:$LiYF_4$ outlined in this paper.

VI. CONCLUSIONS

This research provides strong evidence that more than one cross-relaxation process contributes importantly to nonradiative dynamics in Tm:$LiYF_4$. Stark-state-specific assignments of these cross relaxations (Fig. 13), initiated from multiplets $^1G_4$ and $^3H_4$, yielded good agreement between predicted and observed avalanche thresholds versus temperature and have explained other observations. Comparisons between a simple model and more comprehensive, numerical calculations provided insight into the physical origins of the large peak in fluorescence decay rate of the $^3H_4$ multiplet versus temperature. They showed that excited sublevels with large oscillator strengths provide channels to speed up cross relaxation, but that many sublevels are ineffective in the initiation of cross relaxation because they require high-order vibrational interactions to achieve energy conservation. This justifies the main assumption of our simple two-parameter empirical model, that yielded a remarkably successful fit to the activation data. We conclude that the unusual nonradiative dynamics, which sustain the 648.2 nm avalanche in Tm:$LiYF_4$ arise from the dominance of a small number of excited Stark states, and that this state specificity in thermally-activated cross relaxation has both electronic and vibrational origins.

Another nonradiative process, namely migration, was found to contribute importantly to avalanche efficiency, in agreement with earlier assertions by Ni.[14] The importance of migration can be grasped most easily from the fact that the $^3H_4$ cross-relaxation rate itself is comparable to the lifetime of the $^3F_4$ avalanche state in Tm:$LiYF_4$. Thus, repeated cross relaxations are not capable by themselves of producing high excited-state occupation or the absorption threshold, which is characteristic of an avalanche. A multiplication factor that overcomes this lifetime limitation is needed to explain how incident photons can generate efficient avalanche emission. Measured enhancement factors due to migration in the $^3F_4$ level were consistent with the relative efficiency of avalanche emission in Tm:$LiYF_4$ and Tm:YAG.

ACKNOWLEDGMENTS

We are indebted to G. Huber for providing an important series of Tm:YAG samples and also to N. J. Cockroft and R. M. Macfarlane for various Tm:$LiYF_4$ crystals. At an early stage of this work, partial research support was provided by the Air Force Office of Scientific Research (H. Schlossberg). Funding by the Swiss National Science Foundation is gratefully acknowledged by M.P.H. We are especially thankful to Research Corporation for timely grant support of this project.

*Present address: Gemfire Corporation, 2440 Embarcadero Way, Palo Alto, CA 94304.

[1] J. Chivian, W. Case, and D. Eden, Appl. Phys. Lett. **35**, 124 (1979).

[2] M. Koch, A. Kueny, and W. Case, Appl. Phys. Lett. **56**, 1083 (1990).

[3] A. J. Silversmith, W. Lenth, and R. M. Macfarlane, Appl. Phys. Lett. **51**, 1977 (1987).

[4] R. M. Macfarlane, F. Tong, A. J. Siversmith, and W. Lenth, Appl. Phys. Lett. **52**, 1300 (1988).

[5] D. C. Nguyen, G. E. Faulkner, and M. Dulick, Appl. Opt. **28**, 3553 (1989).

[6] R. A. McFarlane, Appl. Phys. Lett. **54**, 2301 (1989).
[7] M. E. Koch, A. W. Kueny, and W. E. Case, Appl. Phys. Lett. **56**, 1083 (1990).
[8] P. Xie and S. C. Rand, Appl. Phys. Lett. **57**, 1182 (1990).
[9] J. Y. Allain, M. Monerie, and H. Poignant, Electron. Lett. **26**, 262 (1990).
[10] P. Xie and S. C. Rand, Opt. Lett. **17**, 1116 (1992).
[11] H. Ni and S. C. Rand, Opt. Lett. **17**, 1222 (1992).
[12] M. Dennis, J. W. Dixon, and I. Aggarwal, Electron. Lett. **30**, 136 (1994).
[13] M. F. Joubert, S. Guy, and B. Jacquier, Phys. Rev. B **48**, 10 031 (1993).
[14] H. Ni and S. C. Rand, Opt. Lett. **16**, 1424 (1991).
[15] Similar behavior has been reported in Tm:YAG. See G. Armagan, A. M. Buoncristiani, and B. DiBartolo, Opt. Mater. **1**, 11 (1992).
[16] H. Ni, Ph.D. thesis, University of Michigan, Ann Arbor, 1994.
[17] A. Abragam and B. Bleaney, *Electron Paramagnetic Resonance of Transition Ions* (Dover, New York, 1986).
[18] J. H. Van Vleck, Phys. Rev. **57**, 426 (1940).
[19] D. L. Dexter, Phys. Rev. **126**, 1962 (1962).
[20] L. A. Riseberg and H. W. Moos, Phys. Rev. **174**, 429 (1968).
[21] T. Miyakawa and D. L. Dexter, Phys. Rev. B **1**, 2961 (1970).
[22] M. Dulick, G. E. Faulkner, N. J. Cockroft, and D. C. Nguyen, J. Lumin. **48&49**, 517 (1991).
[23] Q. Shu and S. C. Rand, Phys. Rev. B **55**, 8776 (1997).
[24] B. R. Judd, Phys. Rev. **127**, 750 (1962); G. S. Ofelt, J. Chem. Phys. **37**, 511 (1962).
[25] M. F. Reid, J. Chem. Phys. **87**, 2875 (1987).
[26] C. A. Morrison, *Angular Momentum Theory Applied to Interactions in Solids* (Springer, Berlin, 1988).
[27] W. T. Carnall, G. L. Goodman, K. Rajnak, and R. S. Rana, J. Chem. Phys. **90**, 3443 (1989).
[28] D. J. Newman and B. Ng, Rep. Prog. Phys. **52**, 699 (1989).
[29] M. F. Reid and F. S. Richardson, J. Chem. Phys. **79**, 5735 (1983).
[30] P. Blanchfield, J. Phys. C **16**, 3851 (1983).
[31] S. A. Miller, H. E. Rast, and H. H. Caspers, J. Chem. Phys. **52**, 4172 (1970).
[32] M. P. Hehlen, A. Kuditcher, and S. C. Rand, Phys. Rev. Lett. **82**, 3050 (1999).
[33] See for example, D. L. Dexter, J. Chem. Phys. **21**, 836 (1953) or T. Kushida, J. Phys. Soc. Jpn. **34**, 1318 (1973).
[34] R. Orbach, in *Optical Properties of Ions in Crystals*, edited by H. M. Crosswhite and H. W. Moos (Interscience, New York, 1967), p. 445.
[35] P. Blanchfield and G. A. Saunders, J. Phys. C **12**, 4673 (1979).
[36] Q. Shu, Ph.D. thesis, University of Michigan, Ann Arbor, 1996.
[37] A. Lenef, Ph.D. thesis, University of Michigan, Ann Arbor, 1993.
[38] J. R. Salcedo, A. Siegman, D. Dlott, and M. Fayer, Phys. Rev. Lett. **41**, 131 (1978).
[39] S. Guy, M. F. Joubert, B. Jacquier, and S. C. Rand, Ann. Phys. (Paris) **20**, 577 (1995).
[40] A. Kaminskii, *Laser Crystals*, Springer Series in Optical Sciences Vol. 14 (Springer-Verlag, Berlin, 1981), p. 327.